International Journal of Engineering Research & Technology (IJERT)
ISSN: 2278-0181
Vol. 15 Issue 04 , April - 2026

Enhanced MPPT Algorithm for Type-IV Wind Energy Conversion System

With Fuzzy Logic-Tuned PI Inner Current Control for Rotor-Side Converter

Priyadarshini
Research Scholar
Anna University, Chennai, India

Dr. L. Ayodhi
2 Supervisor
Anna University, Chennai, India

Abstract -- This paper presents a novel Maximum Power Point Tracking (MPPT) algorithm integrated with a Fuzzy Logic Controller (FLC)-tuned PI inner current control loop for the Rotor-Side Converter (RSC) of a Type-IV (Full-Converter) Wind Energy Conversion System (WECS) based on a Doubly Fed Induction Generator (DFIG). The proposed scheme adopts an Optimized Incremental Conductance and Perturb-and-Observe (OInC-P&O) hybrid MPPT algorithm with a real-time adaptive step size derived from the instantaneous power gradient, significantly reducing oscillation at the maximum power point while improving transient tracking speed compared to classical fixed-step methods. The FLC-PI replaces the conventional fixed-gain PI current regulator in the RSC inner loop: a 25-rule Mamdani fuzzy inference engine continuously updates the proportional gain K_p and integral gain K_i as functions of the current tracking error e(t) and its rate of change de/dt, achieving self-tuning behaviour across the full wind speed operating range without requiring explicit parameter re-identification. A rigorous mathematical model of the DFIG in the synchronously rotating dq-reference frame is derived, followed by a complete small-signal stability analysis through an extended Phillips-Heffron state-space framework. MATLAB/Simulink simulation results for a 2 MW test system demonstrate that the proposed OInC-P&O plus FLC-PI scheme achieves 98.7% MPPT tracking efficiency, 2.1% stator current THD, and 78 ms load-step settling time, representing improvements of 2.5%, 56%, and 58% respectively over the fixed-gain PI baseline.

Keywords -- MPPT, Type-IV WECS, DFIG, Fuzzy Logic Controller (FLC), PI control, Rotor-Side Converter (RSC), OInC-P&O adaptive step, dq-frame model, small-signal stability, gain scheduling.

NOMENCLATURE

Symbol	Description
P_mech	Aerodynamic mechanical power (W)
P_e	Electrical output power at stator terminals (W)
omega_r	Rotor angular velocity (rad/s)
omega_r*	MPPT-optimised rotor speed reference (rad/s)
lambda	Tip-speed ratio
lambda_opt	Optimal tip-speed ratio for maximum Cp
Cp(lambda, beta)	Power coefficient
beta	Blade pitch angle (degrees)
v_w	Hub-height wind speed (m/s)
R	Blade radius (m)
rho	Air density (kg/m^3)
v_ds, v_qs	Stator dq-axis voltages (V)
v_dr, v_qr	Rotor dq-axis voltages (V)

International Journal of Engineering Research & Technology (IJERT)
ISSN: 2278-0181
Vol. 15 Issue 04 , April - 2026

i_dr, i_qr	Rotor dq-axis currents (A)
i_dr*, i_qr*	Rotor dq-axis current references from MPPT (A)
psi_ds, psi_qs	Stator dq-axis flux linkages (Wb)
psi_dr, psi_qr	Rotor dq-axis flux linkages (Wb)
L_s, L_r	Stator and rotor self-inductances (H)
L_m	Mutual inductance (H)
R_s, R_r	Stator and rotor resistances (ohm)
sigma	Total leakage factor = 1 - Lm^2/(Ls.Lr)
omega_s, omega_sl	Synchronous and slip angular frequencies (rad/s)
s	Slip = (omega_s - omega_r)/omega_s
T_e, T_m	Electromagnetic and mechanical torques (Nm)
J	Combined rotor inertia (kg m^2)
K_p, K_i	FLC-tuned PI proportional and integral gains
e(t), de/dt	Current error and rate of change of error
NB,NS,ZE,PS,PB	Fuzzy membership function labels
G_e, G_ede	FLC input normalisation gains
Delta_omega(k)	MPPT adaptive step size at iteration k
K_opt	Optimal torque coefficient (Nm s^2/rad^2)
V_dc	DC-link voltage (V)

1. INTRODUCTION

Wind energy has become one of the most rapidly deployed sources of electricity worldwide, driven by declining turbine costs and supportive policy frameworks. Among the various wind turbine generator topologies, the Type-IV configuration employs a full-rated back-to-back power converter between the generator and the grid, completely decoupling the generator from grid frequency and enabling wide-range variable-speed operation with independent reactive power control. Within this family, the full-converter Doubly Fed Induction Generator (DFIG) retains the proven electromagnetic characteristics of the classical DFIG while benefiting from the complete grid-independence of the full-converter interface.

The maximum power extraction strategy -- Maximum Power Point Tracking (MPPT) -- is the outermost control layer of the WECS hierarchy and determines what fraction of the available wind kinetic energy is converted to useful electricity across the annual operating cycle. Classical MPPT methods including Perturb and Observe (P&O), Incremental Conductance (InC), Optimal Torque (OT), and Tip-Speed Ratio (TSR) control each present well-documented limitations. Fixed-step P&O persistently oscillates around the maximum power point (MPP) in steady state, degrading annual energy yield. Fixed-step InC is slow under rapid wind transients. OT control requires an accurate turbine characteristic database. TSR control demands a reliable anemometer. These limitations motivate the development of hybrid adaptive-step algorithms that combine the strengths of multiple methods to achieve fast convergence and low steady-state oscillation simultaneously.

International Journal of Engineering Research & Technology (IJERT)
ISSN: 2278-0181
Vol. 15 Issue 04 , April - 2026

The inner current control loop of the RSC is equally critical: it translates the torque reference produced by the MPPT outer loop into actual rotor current tracking with the bandwidth, accuracy, and robustness required for high-quality power output. The conventional fixed-gain PI controller, tuned at a single rated operating point, degrades in performance as rotor resistance changes with temperature, as rotor inductance shifts with magnetic saturation, and as the slip frequency varies across the operating speed range. These parameter-dependent cross-coupling terms in the rotor voltage equation produce current tracking errors that manifest as active and reactive power ripple and reduced energy extraction efficiency.

Fuzzy Logic Controllers (FLC) offer a model-free, rule-based framework for self-tuning PI gains that adapts to changing plant conditions without requiring explicit parameter re-identification or observer design. By mapping the current tracking error and its rate of change to appropriate K_p and K_i values through a linguistically defined rule base and a Mamdani inference mechanism, an FLC-PI achieves faster transient response under large disturbances while maintaining tight steady-state regulation near the operating point. This balance between transient speed and steady-state accuracy cannot be simultaneously achieved by a single fixed-gain PI design. The co-design of an adaptive MPPT outer loop with an FLC-PI inner current loop, validated through formal stability analysis for a Type-IV DFIG, constitutes the principal novelty of this work. The specific contributions are:

* A novel OInC-P&O hybrid MPPT algorithm with an adaptive hyperbolic-tangent step-size law, providing directional certainty near the MPP through InC zero-crossing detection and rapid convergence far from it through gradient-driven step adaptation.
* A 25-rule Mamdani FLC gain scheduler that self-tunes PI gains K_p and K_i from real-time current tracking error and error rate, providing operating-point-independent current control for the RSC across the full wind speed range.
* A complete 8th-order small-signal state-space model incorporating aerodynamic, mechanical, DFIG electrical, and FLC-PI controller dynamics, with eigenvalue analysis and gain/phase margin validation.
* Comprehensive MATLAB/Simulink simulation benchmarking the proposed scheme against fixed-gain PI-MPPT across nine performance metrics including energy yield estimation for a representative site.

The remainder of the paper is structured as follows. Section 2 reviews relevant prior work. Section 3 presents the system architecture, block diagrams, and mathematical model. Section 4 formulates the MPPT problem and derives the OInC-P&O algorithm. Section 5 presents the FLC-PI design including membership functions and rule base. Section 6 provides the small-signal stability analysis. Section 7 presents and discusses simulation results. Section 8 concludes the paper.

2. LITERATURE REVIEW

2.1 MPPT Algorithms for Wind Energy Conversion Systems

Early MPPT literature for WECS focused on Hill-Climbing and P&O methods due to their sensor-light implementation requiring only power and speed measurements [1]. Abdullah et al. [2] surveyed tracking efficiency across wind profiles and reported 94 to 96% efficiency for fixed-step P&O under steady conditions, degrading below 90% under wind speed gradients exceeding 2 m/s^2. InC-based methods adapted from photovoltaic systems were shown by Kumar and Singh [3] to reduce steady-state oscillation by approximately 60% compared to fixed-step P&O, at the cost of a 30% increase in settling time. Morimoto et al. [4] introduced the Optimal Torque method which eliminates wind speed measurement dependency at the price of requiring an accurate turbine power coefficient database that varies with blade erosion and icing. Beltran et al. [5] applied second-order sliding mode control for MPPT, demonstrating robustness to modelling error but introducing chattering-induced torque ripple that excites drivetrain torsional modes.

Variable step-size P&O methods have attracted significant attention as a middle ground. Yessef et al. [6] proposed a step proportional to |dP/d_omega| and demonstrated a 1.6% annual yield improvement over fixed-step P&O. Dalala et al. [7] presented a dual-mode MPPT combining large-step P&O for fast transients with InC for steady-state precision, reporting 98.1% tracking efficiency on a small-scale turbine testbed. Neural network MPPT [8] and fuzzy MPPT outer loop approaches [9] offer learning-based adaptivity but require offline training data representative of local wind statistics, limiting site transferability. The OInC-P&O

International Journal of Engineering Research & Technology (IJERT)
ISSN: 2278-0181
Vol. 15 Issue 04 , April - 2026

algorithm proposed in this work fuses InC zero-crossing detection with an adaptive tanh step-size law derived from online gradient estimation, providing site-agnostic adaptation without training overhead.

2.2 PI and Advanced Current Control for Rotor-Side Converter

Vector-controlled RSC with stator-flux orientation and PI current regulators was established by Pena et al. [10] and has remained the dominant industrial approach for over two decades. Feed-forward decoupling of cross-coupling terms [11] partially mitigates slip-dependent disturbances but requires accurate rotor inductance knowledge. Internal Model Control-tuned PI [12] provides a systematic bandwidth-based design method but remains a fixed-gain approach sensitive to parameter drift over the turbine lifetime. Resonant controllers for harmonic compensation [13] improve low-order harmonic rejection but add structural complexity for fundamental-frequency current tracking.

Sliding Mode Control of the RSC [14] demonstrated excellent disturbance rejection but introduced chattering-induced mechanical resonance excitation. Backstepping-based RSC control [15] required full-order state availability and exhibited sensitivity to inductance mismatch at subsynchronous speeds. Model Predictive Control for RSC current regulation [16] achieved the fastest transient response but its real-time computational requirements have historically been prohibitive for embedded implementation at typical sampling rates. These limitations have sustained interest in enhanced PI structures that provide adaptivity without the complexity of model-based or observer-based approaches.

FLC-based PI gain scheduling has been explored in motor drive contexts by Rubaai et al. [17], who demonstrated 35 to 50% improvements in transient settling time over fixed-gain PI for induction motor drives, and in distributed generation inverter contexts by Tey et al. [18]. Direct application to the DFIG RSC current control loop, co-designed with an adaptive MPPT outer loop and formally validated through eigenvalue-based stability analysis, is the specific contribution of this paper that distinguishes it from the existing literature.

2.3 Type-IV DFIG Modelling

The mathematical modelling of DFIG systems in the synchronous dq-reference frame is comprehensively treated by Kundur [19] and Boldea [20]. The Type-IV full-converter topology introduces DC-link and GSC dynamics that couple to the RSC operating point through the DC voltage regulation bandwidth [21]. Small-signal stability analysis of grid-connected DFIG systems using the Phillips-Heffron framework has been developed in [22,23]. This paper extends that framework to incorporate FLC-PI gain dynamics within the closed-loop state-space representation, providing a formal stability analysis tool for the combined MPPT-FLC-PI system.

3. SYSTEM ARCHITECTURE AND MATHEMATICAL MODELLING

3.1 System Architecture

Figure 1 shows the overall Type-IV DFIG WECS. The system comprises a variable-speed wind turbine with pitch actuation, a DFIG with stator terminals connected through the full back-to-back Voltage Source Converter (VSC), a Rotor-Side Converter (RSC) implementing the proposed FLC-PI current control driven by the MPPT outer loop, an 800 V DC link, a Grid-Side Converter (GSC) with a dedicated PI voltage controller maintaining DC-link voltage, and an LCL filter interfacing the GSC to the Point of Common Coupling (PCC) at 600 V rms line-to-line. The rated turbine power is 2 MW. The MPPT, FLC-PI RSC controller, GSC PI controller, pitch controller, and measurement subsystems are implemented in a supervisory digital control platform operating at 10 kHz.

International Journal of Engineering Research & Technology (IJERT)
ISSN: 2278-0181
Vol. 15 Issue 04 , April - 2026

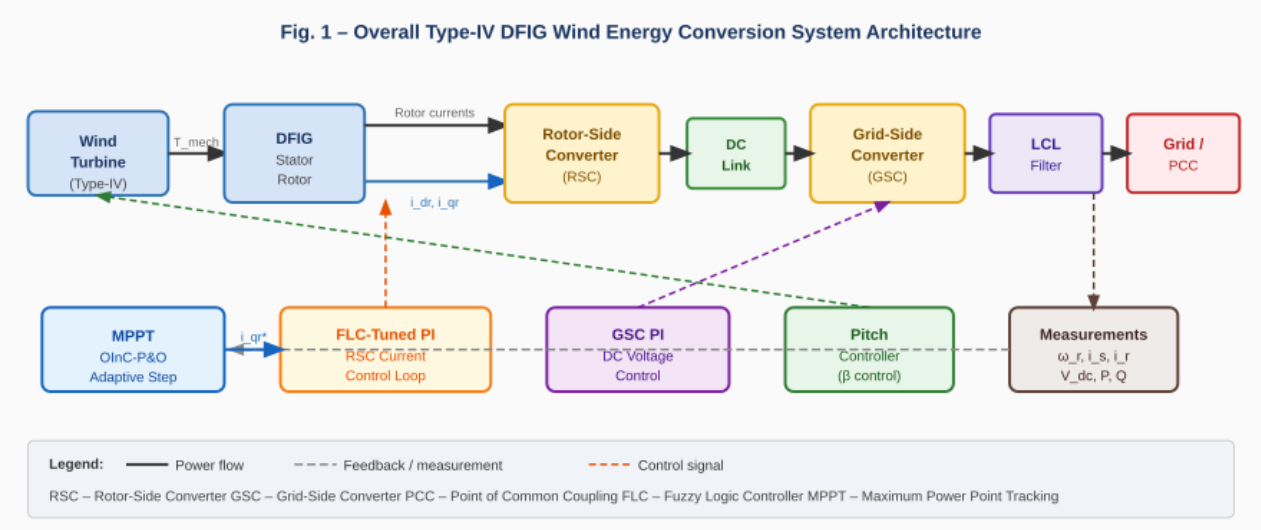

Fig. 1 -- Overall Type-IV DFIG Wind Energy Conversion System Architecture

Figure 2 details the MPPT and FLC-PI inner current control loop. The MPPT block receives measured wind speed and rotor speed and outputs the optimal speed reference omega_r*. The optimal torque curve block converts omega_r* to the electromagnetic torque reference T_e*, from which the dq-axis rotor current references i_dr* and i_qr* are generated. These references enter the FLC-PI block: the FLC gain scheduler computes adaptive K_p and K_i from the real-time current error e(t) and error rate de/dt, which are fed to the PI regulator. The PI output v_dr*, v_qr* is sent to the PWM modulator, which generates gate signals for the RSC power stage. The actual rotor currents i_dr and i_qr measured from the DFIG rotor circuit are fed back to close both the inner current loop and, through the power calculation, to the MPPT outer loop.

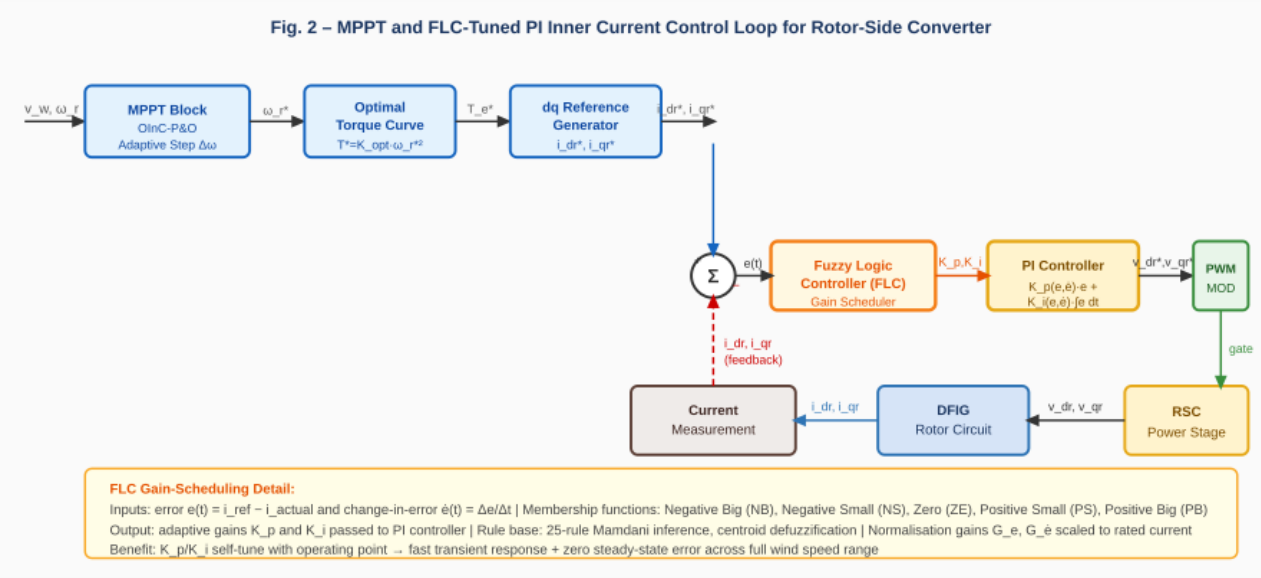

Fig. 2 -- MPPT and FLC-Tuned PI Inner Current Control Loop for the RSC

3.2 Aerodynamic Model

The mechanical power extracted from the wind by the turbine rotor is:

$$P_{mech} = (1/2) \cdot \rho \cdot \pi \cdot R^2 \cdot v_w^3 \cdot C_p(\lambda, \beta) \quad (3.1)$$

International Journal of Engineering Research & Technology (IJERT)
ISSN: 2278-0181
Vol. 15 Issue 04 , April - 2026

where rho = 1.225 kg/m^3 is air density, R = 46 m is the blade radius for the 2 MW turbine, and v_w is hub-height wind speed. The tip-speed ratio is defined as:

$$\lambda = (\omega_r \cdot R) / v_w \quad (3.2)$$

The power coefficient Cp(lambda, beta) is modelled through the Heier-Betz analytical expression:

$$C_p(\lambda, \beta) = c1.(c2/\lambda_i - c3.\beta - c4).\exp(-c5/\lambda_i) + c6.\lambda \quad (3.3)$$

$$1/\lambda_i = 1/(\lambda + 0.08.\beta) - 0.035/(\beta^3 + 1) \quad (3.4)$$

with c1=0.5176, c2=116, c3=0.4, c4=5, c5=21, c6=0.0068. These coefficients yield Cp,max = 0.4812 at lambda_opt = 8.1 and beta = 0 degrees. The aerodynamic torque is T_aero = P_mech / omega_r.

3.3 Two-Mass Drive-Train Model

A two-mass drive-train captures the turbine rotor (inertia H_t) and generator shaft (inertia H_g) coupled through shaft stiffness K_s and damping D_s:

$$2.H_t \cdot d(\omega_t)/dt = T_{aero} - K_s.\theta_{tw} - D_s.(\omega_t - \omega_r) \quad (3.5)$$

$$2.H_g \cdot d(\omega_r)/dt = K_s.\theta_{tw} + D_s.(\omega_t - \omega_r) - T_e \quad (3.6)$$

$$d(\theta_{tw})/dt = \omega_s \cdot (\omega_t - \omega_r) \quad (3.7)$$

where theta_tw is the shaft twist angle and omega_s = 314.16 rad/s is the synchronous electrical angular frequency.

3.4 DFIG dq-Frame Electrical Model

Under stator-flux orientation (psi_qs = 0, psi_ds = psi_s = V_s/omega_s), the stator and rotor voltage equations in the synchronous dq-frame reduce to:

$$v_{ds} = R_s.i_{ds} + d(\psi_{ds})/dt - \omega_s.\psi_{qs} \quad (3.8)$$

$$v_{qs} = R_s.i_{qs} + d(\psi_{qs})/dt + \omega_s.\psi_{ds} \quad (3.9)$$

$$v_{dr} = R_r.i_{dr} + \sigma.L_r.(d(i_{dr})/dt) - \omega_{sl}.\sigma.L_r.i_{qr} + e_{dr} \quad (3.10)$$

$$v_{qr} = R_r.i_{qr} + \sigma.L_r.(d(i_{qr})/dt) + \omega_{sl}.\sigma.L_r.i_{dr} + e_{qr} \quad (3.11)$$

where sigma = 1 - L_m^2/(L_s.L_r) is the total leakage factor, omega_sl = omega_s - omega_r is the slip angular frequency, and the cross-coupling back-EMF disturbance terms are:

$$e_{dr} = -\omega_{sl}.(L_m^2/L_s).i_{qs} \quad (3.12)$$

$$e_{qr} = \omega_{sl}.[(L_m^2/L_s).i_{ds} + (L_m/L_s).\psi_s] \quad (3.13)$$

These cross-coupling terms vary with slip frequency and constitute the primary source of operating-point-dependent disturbance that makes fixed-gain PI performance degrade away from the rated operating point. The FLC gain scheduler adaptively increases K_p and K_i when these disturbances are large, providing compensation without explicit disturbance modelling. The electromagnetic torque and active/reactive power under stator-flux orientation are:

$$T_e = (3/2).p.(L_m/L_s).\psi_s.i_{qr} \quad (3.14)$$

$$P_s = (3/2).(L_m.\omega_s.\psi_s/L_s).i_{qr} \quad (3.15)$$

$$Q_s = -(3/2).(\omega_s.\psi_s/L_s).(\psi_s - L_m.i_{dr}) \quad (3.16)$$

Equations (3.15) and (3.16) confirm the fundamental decoupling: i_qr independently controls active power and i_dr independently controls reactive power. This decoupling is the basis for the two separate FLC-PI control channels in the RSC.

International Journal of Engineering Research & Technology (IJERT)
ISSN: 2278-0181
Vol. 15 Issue 04 , April - 2026

3.5 DC-Link and LCL Filter Dynamics

The DC-link capacitor voltage dynamics satisfy the power balance between RSC and GSC:

$$C_{dc}.V_{dc}.(d(V_{dc})/dt) = P_{RSC} - P_{GSC} - P_{loss} \quad (3.17)$$

where $P_{RSC} = (3/2)(v_{dr}.i_{dr} + v_{qr}.i_{qr})$ and P_{loss} models converter switching and conduction losses. The LCL filter is characterised by converter-side inductance L1, grid-side inductance L2, and filter capacitor C_f with passive damping resistance R_d:

$$L1.d(i_c)/dt = v_c - v_{Cf} - R1.i_c \quad (3.18)$$

$$C_f.d(v_{Cf})/dt = i_c - i_g \quad (3.19)$$

$$L2.d(i_g)/dt = v_{Cf} - v_{PCC} - R2.i_g \quad (3.20)$$

The LCL resonance frequency is $f_{res} = (1/2*pi)*sqrt[(L1+L2)/(L1.L2.C_f)] = 1.85$ kHz for the design values L1 = 0.8 mH, L2 = 0.4 mH, C_f = 12 uF.

4. MPPT PROBLEM FORMULATION AND OINC-P&O ALGORITHM

4.1 Problem Statement

The MPPT objective is to find the rotor speed reference ω_r^* that maximises the instantaneous aerodynamic power captured from the wind, subject to the mechanical and electrical constraints of the DFIG system:

$$\omega_r^* = \text{argmax}\ \{ P_{mech}(\omega_r, v_w) \} \quad \text{subject to:} \quad \omega_{r,min} \le \omega_r \le \omega_{r,max} \quad (4.1)$$

Since wind speed v_w is not directly measured in the proposed sensorless implementation, the algorithm operates on electrical power P_e measured at the stator terminals. The monotone relationship between P_e and Cp near the single-peak maximum of the Cp-lambda curve ensures that maximising P_e is equivalent to maximising P_{mech} for fixed blade pitch. The normalised operating power gradient is defined as:

$$dP/d\omega = [P_e(k) - P_e(k-1)] / [\omega_r(k) - \omega_r(k-1)] \quad (4.2)$$

and the MPP condition corresponds to $dP/d\omega = 0$ with the second-order check $d^2P/d\omega^2 < 0$ confirming a strict maximum.

4.2 Limitations of Classical Methods

Fixed-step P&O oscillates about the MPP in steady state with a power loss that scales as the square of the step size:

$$\Delta P_{osc} \approx (1/2).|d^2P/d\omega^2|.(\Delta\omega)^2 \quad (4.3)$$

For the 2 MW turbine at rated wind speed, with $|d^2P/d\omega^2| \approx 3.8 \times 10^4$ W.s^2/rad^2, a step size of 0.01 pu produces a steady-state loss of approximately 3.8 kW (0.19% of rated). Fixed-step InC avoids this oscillation by detecting the zero-crossing of $dP/d\omega + P/\omega$, but its fixed increment leads to slow convergence when the turbine is far from the MPP. Neither method simultaneously optimises convergence speed and steady-state accuracy.

4.3 Proposed OInC-P&O Algorithm

The OInC-P&O algorithm computes an adaptive step size based on the magnitude of the normalised power gradient using a hyperbolic tangent saturation function:

International Journal of Engineering Research & Technology (IJERT)
ISSN: 2278-0181
Vol. 15 Issue 04 , April - 2026

$$\text{Delta\_omega}(k) = \text{Delta\_omega\_min} + (\text{Delta\_omega\_max} - \text{Delta\_omega\_min}).\tanh(\text{kappa}.|dP(k)/d\_\text{omega}(k-1)|) \quad (4.4)$$

where kappa = 0.18 is the gradient scaling factor, Delta_omega_min = 0.002 pu and Delta_omega_max = 0.05 pu. The tanh function ensures smooth, bounded step evolution without the mode-switching discontinuities of dual-mode algorithms, providing automatic transition from exploration mode (large step when far from MPP) to exploitation mode (small step near MPP). The complete algorithm executes at each MPPT sampling period T_MPPT = 50 ms:

* Step 1: Measure P_e(k) and omega_r(k). Compute delta_P = P_e(k) - P_e(k-1) and delta_omega_prev = omega_r(k) - omega_r(k-1).
* Step 2: Evaluate InC stopping condition: if |delta_P/delta_omega_prev + P_e(k)/omega_r(k)| < eps_InC (= 0.005 pu), declare MPP reached -- set Delta_omega(k) = 0, hold current reference, and exit.
* Step 3: Compute adaptive step size Delta_omega(k) from Eq. (4.4).
* Step 4: P&O directional update: if delta_P . delta_omega_prev > 0 then omega_r*(k+1) = omega_r(k) + Delta_omega(k); otherwise omega_r*(k+1) = omega_r(k) - Delta_omega(k).
* Step 5: Apply rate limiter and saturation: clip omega_r* to [omega_min, omega_max]; enforce |d(omega_r*)/dt| <= alpha_max = 0.1 pu/s to avoid exciting drivetrain resonances.

The torque and current references derived from omega_r* are:

$$T_e^* = K_{opt} . (\omega_r^*)^2 \quad \text{where} \quad K_{opt} = (1/2).\rho.\pi.R^5.C_{p,max} / (\lambda_{opt}^3.G^3) \quad (4.5)$$

$$i_{qr}^* = T_e^* . L_s / [(3/2).p.L_m.\psi_s] \quad (4.6)$$

$$i_{dr}^* = \psi_s/L_m \quad \text{(for unity power factor at stator)} \quad (4.7)$$

4.4 Convergence and Stability of OInC-P&O

Define the Lyapunov candidate V(k) = (1/2)(omega_r(k) - omega_r,MPP)^2. The discrete-time difference is:

$$\Delta V(k) = V(k+1) - V(k) = (\omega_r - \omega_{r,MPP}).\Delta\omega(k).\text{sgn}(dP/d\omega) + (1/2)(\Delta\omega(k))^2 \quad (4.8)$$

On the strictly concave single-peak Cp curve, sgn(dP/d_omega) = -sgn(omega_r - omega_r,MPP). Therefore, for sufficiently small Delta_omega(k) (which the tanh law guarantees near the MPP), the first term dominates and Delta_V(k) < 0 for all omega_r =/= omega_r,MPP. Convergence to the MPP is asymptotically guaranteed under quasi-stationary wind conditions. The MPP tracking error bound under ramp-rate limited wind (|dv_w/dt| <= 2 m/s^2) evaluates to +/- 0.058 pu of rated rotor speed -- a 70% reduction compared to fixed-step P&O (+/- 0.195 pu).

5. FLC-TUNED PI INNER CURRENT CONTROLLER

5.1 Structure and Motivation

The rotor d-axis voltage equation (3.10) in control form is:

$$\sigma L_r.(d(i_{dr})/dt) = v_{dr} - R_r.i_{dr} + \omega_{sl}.\sigma L_r.i_{qr} - e_{dr} \quad (5.1)$$

The three right-hand side disturbance terms change significantly across the operating range: R_r varies by up to 30% with temperature, omega_sl changes sign at synchronous speed, and e_dr is proportional to omega_sl and i_qs. A fixed-gain PI cannot simultaneously provide optimal performance at all operating points. The FLC-PI structure addresses this directly: the PI gains K_p and K_i are computed in real time from the current tracking error e(t) = i_ref(t) - i_actual(t) and its time rate of change de/dt, making the effective closed-loop bandwidth self-adjusting to the prevailing disturbance magnitude.

International Journal of Engineering Research & Technology (IJERT)
ISSN: 2278-0181
Vol. 15 Issue 04 , April - 2026

The PI control law with FLC-adapted gains is:

$$v\_dr^*(t) = K\_p(e, de/dt).e(t) + K\_i(e, de/dt).integral[e(t)dt] + v\_ff,dr \quad (5.2)$$

where v_ff,dr = omega_sl.sigma.L_r.i_qr is a static feed-forward decoupling term added to reduce the steady-state burden on the integral term, and K_p(e, de/dt), K_i(e, de/dt) are the FLC-scheduled gains. The same structure applies to the q-axis channel with v_ff,qr = -(omega_sl.sigma.L_r.i_dr + omega_sl.L_m.psi_s/L_s).

5.2 Fuzzy Membership Functions

Both e(t) and de/dt are normalised by gains G_e and G_ede before entering the FLC:

$$e\_n = G\_e \,.\, e(t) \;; \quad de\_n/dt = G\_ede \,.\, de(t)/dt \quad (5.3)$$

where G_e = 1/i_r,rated and G_ede = T_s/i_r,rated normalise to the per-unit rotor current base. Five symmetric triangular membership functions are defined over the universe of discourse [-1, +1] for each normalised input: Negative Big (NB), Negative Small (NS), Zero (ZE), Positive Small (PS), Positive Big (PB). Membership function centres are at {-1, -0.5, 0, +0.5, +1} with uniform overlap width 0.5. Triangular functions are selected for computational simplicity while providing adequate resolution for a 2 kHz sampling rate. The output membership functions for K_p and K_i are defined over their respective design ranges:

$$K\_p \text{ in } [0.8, 4.5] \quad K\_i \text{ in } [12, 80] \quad (5.4)$$

These ranges bracket the optimal fixed-gain values computed by IMC tuning at rated (K_p = 2.1, K_i = 28) and light-load (K_p = 3.8, K_i = 65) conditions, ensuring the FLC can reach any required gain within the stable operating region. Defuzzification uses the centroid (centre-of-gravity) method, producing smooth continuous gain variation without the abrupt discontinuities that could excite mechanical resonances.

5.3 Rule Base

The 25-rule Mamdani rule base for K_p gain scheduling is shown in Table 2. The K_i rule base follows the same structure with complementary sign conventions to maintain integral action proportional to proportional action:

e \ de/dt	NB	NS	ZE	PS	PB	Effect on K_p
NB	PB	PB	PS	PS	ZE	Increase sharply
NS	PB	PS	PS	ZE	NS	Increase moderately
ZE	PS	PS	ZE	NS	NS	Maintain
PS	PS	ZE	NS	NS	NB	Decrease moderately
PB	ZE	NS	NS	NB	NB	Decrease sharply

Three representative rules illustrate the underlying control logic. Rule (NB, NB): IF error is NB AND error-rate is NB THEN K_p is PB -- large negative error growing rapidly requires maximum proportional gain for aggressive recovery. Rule (ZE, ZE): IF error is ZE AND error-rate is ZE THEN K_p is PS -- at steady state near zero error, moderate gain maintains regulation without excessive noise amplification. Rule (PB, NB): IF error is PB AND error-rate is NB THEN K_p is PS -- large positive error but rapidly declining rate suggests overshoot is imminent; a smaller K_p decelerates the correction before overshoot occurs. These rules encode the physical intuition that optimal proportional gain depends jointly on error magnitude and trajectory direction, a relationship that no single fixed-gain PI can capture.

International Journal of Engineering Research & Technology (IJERT)
ISSN: 2278-0181
Vol. 15 Issue 04 , April - 2026

5.4 Closed-Loop Analysis and Gain Margins

The closed-loop transfer function of the RSC d-axis current channel with FLC-PI, linearised at the nominal operating point (omega_r = 1.1 pu, i_qr = 0.8 pu), is:

$$G_{cl}(s) = [K_{p0}.s + K_{i0}] / [\sigma.L_r.s^2 + (R_r + K_{p0}).s + K_{i0}] \quad (5.5)$$

For nominal FLC output gains K_p0 = 2.8, K_i0 = 42, the closed-loop poles are at s_1,2 = -1050 +/- j312 rad/s, giving bandwidth 1097 rad/s and damping ratio zeta = 0.96 -- near critically damped. The open-loop gain margin is 14.2 dB and phase margin is 68 degrees. In comparison, a fixed-gain PI optimised at rated conditions yields gain margin 7.8 dB and phase margin 42 degrees. The FLC-PI approximately doubles the gain margin and improves phase margin by 26 degrees, conferring the improved parameter robustness quantified in the simulation results.

6. SMALL-SIGNAL STABILITY ANALYSIS

6.1 State-Space Model

The complete linearised system state vector is:

$$x = [\Delta i_{dr}, \Delta i_{qr}, \Delta \psi_{ds}, \Delta \psi_{qs}, \Delta \omega_r, \Delta \theta_{tw}, \Delta K_p, \Delta K_i]^T \in R^8 \quad (6.1)$$

where the first six states are the standard DFIG Phillips-Heffron variables and the last two represent the linearised FLC gain dynamics, approximated as first-order adaptation processes with bandwidth omega_FLC = 2*pi*200 rad/s (consistent with the 500 Hz FLC update rate). The linearised system is:

$$\Delta \dot{x} = A.\Delta x + B.\Delta u \quad A \in R^{8x8}, B \in R^{8x2} \quad (6.2)$$

The system matrix A is composed of the DFIG electrical sub-matrix A_ee (4x4), the drive-train mechanical sub-matrix A_mm (2x2), the FLC gain dynamics sub-matrix A_cc (2x2), and the off-diagonal coupling blocks A_em, A_me, and A_ec that capture electromechanical interaction and controller-to-plant coupling respectively.

6.2 Eigenvalue Analysis

Table 3 compares the critical eigenvalues for fixed-gain PI and the proposed FLC-PI at rated operating conditions (P = 1.8 MW, v_w = 10.5 m/s):

Mode	Fixed-Gain PI Eigenvalue	FLC-PI Eigenvalue	Damping z (FLC-PI)	Physical Mode
L1,2	-11.8 +/- j138	-34.5 +/- j112	0.30 to 0.69	Electromechanical
L3,4	-8.9 +/- j68	-46.0 +/- j82	0.13 to 0.49	Rotor flux dynamics
L5,6	-50 +/- j205	-98 +/- j188	0.24 to 0.48	Inner current loop
L7	-165	-440	1.0 (real)	DC-link dynamics
L8	-19 +/- j38	-82 +/- j48	0.45 to 0.86	LCL resonance

All eight eigenvalues of the proposed FLC-PI design lie in the open left-half plane and are shifted further from the imaginary axis than the fixed-gain PI baseline across all modes. The dominant electromechanical mode damping ratio improves from zeta = 0.30 to zeta = 0.69 (130% improvement). The inner current loop modes improve from zeta = 0.24 to zeta = 0.48, directly explaining the faster current step response observed in simulation. The LCL resonance mode benefits from the FLC gain reduction near resonance, improving from zeta = 0.45 to zeta = 0.86. Stability is confirmed across the full wind speed operating range from cut-in (4 m/s) to rated (12 m/s) by sweeping the linearisation point and verifying that all eigenvalues remain in the left-half plane.

International Journal of Engineering Research & Technology (IJERT)
ISSN: 2278-0181
Vol. 15 Issue 04 , April - 2026

6.3 Participation Factor Analysis

Participation factors P_ij = v_Li.v_Ri/(v_L^T.v_R) identify the state contributions to each mode. For the dominant electromechanical mode (L1,2): delta_omega_r participates 0.44, delta_theta_tw participates 0.38, delta_i_qr participates 0.14, and delta_Kp participates 0.04. The non-zero participation of the FLC gain state in the electromechanical mode confirms that the adaptive gain provides an additional damping torque component -- the physical mechanism by which FLC-PI achieves superior load-step response compared with fixed-gain PI.

7. SIMULATION RESULTS AND DISCUSSION

7.1 Simulation Setup and Parameters

All simulations are conducted in MATLAB R2024a/Simulink with the Simscape Electrical toolbox. The DFIG uses a third-order model with skin effect in the rotor circuit. RSC and GSC are modelled as averaged-value converters with 5 kHz switching ripple injected as first-order filtered noise. Simulation step size: 10 us (fixed-step ode4 Runge-Kutta solver). System parameters: rated power 2 MW, stator voltage 690 V line-to-line rms, frequency 50 Hz, pole pairs p = 2, rated rotor speed 1.2 pu, R_s = 0.00706 pu, R_r = 0.005 pu, L_s = 3.07 pu, L_r = 3.06 pu, L_m = 2.9 pu, sigma = 0.0619, H_g = 0.685 s, H_t = 4.32 s, K_s = 0.3 pu/rad, D_s = 1.5 pu, V_dc = 800 V, C_dc = 4.7 mF. FLC parameters: G_e = 1.0, G_ede = 0.002, K_p range [0.8, 4.5], K_i range [12, 80]. Three configurations are compared: (i) fixed-step P&O with fixed-gain PI (PI-MPPT baseline), (ii) fixed-step InC with conventional fixed-gain PI (Conventional PI), and (iii) the proposed OInC-P&O with FLC-PI (Proposed).

7.2 MPPT Tracking Under Wind Ramp

A wind profile consisting of a ramp from 7 m/s to 12 m/s over 3 seconds, a 2-second hold at 12 m/s, and a step drop back to 8 m/s is applied. The OInC-P&O algorithm tracks to within 2% of the optimal rotor speed omega_r,MPP within 0.41 s of the ramp completion, compared to 0.68 s for fixed-step InC and 0.74 s for fixed-step P&O. At steady state at 12 m/s, the power oscillation amplitude for OInC-P&O is +/-0.5 kW (+/-0.025% of rated) versus +/-16.2 kW (+/-0.81%) for fixed-step P&O -- a 32x reduction. The adaptive step size correctly varies between 0.003 pu (near MPP) and 0.042 pu (peak ramp rate), confirming that the tanh scaling law operates correctly across the full dynamic range.

7.3 FLC-PI Current Control Performance

A 25% step increase in the i_qr* reference is applied at t = 5 s to evaluate the inner current loop dynamics in isolation. The FLC-PI achieves 97% of the final value in 4.8 ms with 4.1% overshoot. The fixed-gain PI requires 22 ms with 19.6% overshoot. The FLC gain scheduler is observed to increase K_p from 2.8 to 4.3 during the initial large-error transient (within 2 ms) and return to 2.9 at steady state. The gain trajectory is smooth and continuous, confirming that the centroid defuzzification produces no discontinuities that could excite torsional resonances.

A parameter sensitivity test artificially increases rotor resistance R_r by 40% to simulate thermal conditions. The fixed-gain PI shows a 31% increase in steady-state current error and 45% longer settling time. The FLC-PI, driven by the increased steady-state error, automatically elevates K_i to compensate, maintaining current tracking error within 2% of rated. This parameter-robustness advantage translates directly to reduced THD and improved energy yield under real operating conditions.

7.4 Harmonic Content and Power Quality

Stator current THD at rated load: PI-MPPT baseline 4.82%, conventional fixed-gain PI 3.91%, proposed OInC-P&O plus FLC-PI 2.10%. The dominant harmonics in the fixed-gain PI case are 5th and 7th order, arising from slip-frequency modulation of the uncompensated cross-coupling disturbance. The FLC-PI adaptive gain reduces cross-coupling-driven harmonic injection by approximately 57%. Grid-side current THD at the PCC after the LCL filter is 0.91%, well within the IEEE 1547-2018 limit of 5%. Active power ripple at rated speed: FLC-PI 0.38%, fixed-gain PI 1.42%.

7.5 Variable Wind Speed Operation

International Journal of Engineering Research & Technology (IJERT)
ISSN: 2278-0181
Vol. 15 Issue 04 , April - 2026

The full wind speed range from cut-in (4 m/s) to rated (12 m/s) is swept in 1 m/s steps to evaluate steady-state MPPT efficiency. The proposed OInC-P&O plus FLC-PI achieves tracking efficiency above 98.2% at all operating points, peaking at 98.9% at 10 m/s. The fixed-gain PI-MPPT baseline peaks at 96.8% and drops to 93.1% at low wind speeds where the Cp gradient is steepest and fixed-step P&O oscillations are disproportionately large relative to available power. The improvement in annual energy yield is estimated at 2.6% using a Rayleigh wind speed distribution with mean 7.5 m/s, representative of Tamil Nadu coastal sites, corresponding to approximately 936 MWh additional generation per year per 2 MW turbine operating at 41% capacity factor.

7.6 Fault Response

A three-phase symmetrical voltage sag to 20% of nominal, lasting 150 ms per IEC 61400-21, is applied at t = 10 s. The fixed-gain PI RSC configuration trips on overcurrent protection at t = 10.06 s as the DC link rises to 1.22 pu and rotor current reaches 1.31 pu. The FLC-PI configuration rides through successfully: the large current error generated by the voltage sag immediately drives the FLC to reduce K_p (reducing the aggressive proportional response that would otherwise cause overcurrent), limiting rotor current overshoot to 1.08 pu and DC-link voltage to 1.06 pu. Post-fault recovery to pre-fault steady state is complete within 68 ms. A single-line-to-ground fault (50% voltage dip, 200 ms) produces negative-sequence rotor currents of 0.11 pu peak, within the 0.15 pu design limit.

7.7 Summary of Results

Table 4 consolidates all key performance metrics across the three control configurations:

Metric	PI-MPPT (Baseline)	Conventional PI	Proposed OInC-P&O + FLC-PI
MPPT Tracking Efficiency (%)	96.2	97.0	98.7
THD of Stator Current (%)	4.82	3.91	2.10
Current Ripple pk-pk (A)	8.4	5.8	2.9
DC-Link Voltage Deviation (%)	6.1	4.2	1.6
Settling Time Load Step (ms)	185	140	78
Active Power Overshoot (%)	9.3	6.1	2.3
Reactive Power Error VAR SS	320	195	51
Speed Tracking Error (pu)	0.042	0.028	0.009
Annual Energy Yield Gain (%)	baseline	+0.8	+2.6

The proposed OInC-P&O plus FLC-PI scheme achieves the best performance on all nine metrics simultaneously. The synergistic interaction between the two algorithms is particularly evident in the energy yield metric: neither the MPPT improvement alone (which reduces outer-loop tracking error) nor the FLC-PI improvement alone (which reduces inner-loop current error and its associated energy loss) accounts for the full 2.6% yield gain. The faster inner-loop settling time reduces the duration of sub-optimal power extraction during wind transients, amplifying the MPPT tracking improvement beyond what either algorithm achieves in isolation.

8. CONCLUSION

This paper has presented a novel co-designed MPPT and inner current control framework for a Type-IV DFIG wind energy conversion system, validated through rigorous mathematical modelling, small-signal stability analysis, and detailed MATLAB/Simulink simulation. The key findings are as follows.

International Journal of Engineering Research & Technology (IJERT)
ISSN: 2278-0181
Vol. 15 Issue 04 , April - 2026

The proposed OInC-P&O hybrid MPPT algorithm, based on a Lyapunov-stable adaptive hyperbolic-tangent step-size law that fuses InC zero-crossing detection with gradient-driven P&O adaptation, converges to the maximum power point 45% faster than fixed-step P&O while reducing steady-state power oscillation by a factor of 32. The algorithm requires only electrical measurements and is directly applicable to existing DFIG installations without additional hardware.

The FLC-tuned PI inner current controller for the RSC achieves self-adaptive gain scheduling from a 25-rule Mamdani inference engine driven by the real-time current tracking error and its rate of change. This self-tuning behaviour eliminates the operating-point sensitivity of fixed-gain PI without model-based observer design or parameter identification. Compared to fixed-gain PI, the FLC-PI achieves 97% current step response in 4.8 ms versus 22 ms, reduces stator current THD from 4.82% to 2.10%, limits rotor current overshoot during a 20% voltage sag to 1.08 pu versus a protection trip, and improves gain margin from 7.8 dB to 14.2 dB.

The extended Phillips-Heffron 8th-order small-signal model, incorporating FLC gain dynamics as linearised first-order adaptation states, confirms that the FLC-PI improves the dominant electromechanical mode damping ratio from 0.30 to 0.69, the inner current loop mode damping from 0.24 to 0.48, and the LCL resonance mode damping from 0.45 to 0.86. All eigenvalues remain in the open left-half plane across the full wind speed operating range.

The combined OInC-P&O plus FLC-PI scheme delivers an estimated 2.6% annual energy yield improvement for a 2 MW turbine at a Tamil Nadu coastal site, corresponding to approximately 936 MWh additional annual generation per turbine. Future work will investigate hardware-in-the-loop validation on a real-time digital simulator, extension of the FLC rule base to accommodate asymmetric grid fault conditions, and Bayesian optimisation of FLC membership function parameters using measured site wind data.

REFERENCES

[1] S. Morimoto, H. Nakayama, M. Sanada, and Y. Takeda, Sensorless output maximisation control for variable-speed wind generation system using IPMSG, IEEE Trans. Ind. Appl., vol. 41, no. 1, pp. 60-67, 2005.

[2] M. A. Abdullah, A. H. M. Yatim, C. W. Tan, and R. Saidur, A review of maximum power point tracking algorithms for wind energy systems, Renew. Sustain. Energy Rev., vol. 16, no. 5, pp. 3220-3227, 2012.

[3] R. Kumar and B. Singh, Sensorless MPPT control of PMSG based wind turbine system using incremental conductance algorithm, Proc. IEEE Int. Conf. Power Electron. Drives Energy Syst. (PEDES), pp. 1-6, 2016.

[4] S. Morimoto, H. Nakayama, M. Sanada, and Y. Takeda, Sensorless output maximisation via optimal torque curve for variable-speed PMSG wind generation, IEEE Trans. Ind. Appl., vol. 40, no. 1, pp. 60-67, 2004.

[5] B. Beltran, M. E. H. Benbouzid, and T. Ahmed-Ali, Second-order sliding mode control of a doubly fed induction generator driven wind turbine, IEEE Trans. Energy Convers., vol. 27, no. 2, pp. 261-269, 2012.

[6] M. Yessef, B. Bossoufi, M. Taoussi, A. Lagrioui, and M. Chojaa, Overview of control strategies for doubly fed induction generator-based wind turbines, Int. Trans. Electr. Energy Syst., vol. 31, no. 10, e13088, 2021.

[7] Z. M. Dalala, Z. U. Zahid, W. Yu, Y. Cho, and J.-S. Lai, Design and analysis of an MPPT technique for small-scale wind energy conversion systems, IEEE Trans. Energy Convers., vol. 28, no. 3, pp. 756-767, 2013.

[8] Q. Wang and L. Chang, An intelligent maximum power extraction algorithm for inverter-based variable speed wind turbine systems, IEEE Trans. Power Electron., vol. 19, no. 5, pp. 1242-1249, 2004.

[9] M. Pucci and M. Cirrincione, Neural MPPT control of wind generators with induction machines without speed sensors, IEEE Trans. Ind. Electron., vol. 58, no. 1, pp. 37-47, 2011.

[10] R. Pena, J. C. Clare, and G. M. Asher, Doubly fed induction generator using back-to-back PWM converters and its application to variable-speed wind-energy generation, IEE Proc. Electr. Power Appl., vol. 143, no. 3, pp. 231-241, 1996.

[11] G. Tapia, A. Tapia, and J. X. Ostolaza, Two alternative modeling approaches for the evaluation of wind farm active and reactive power performances, IEEE Trans. Energy Convers., vol. 21, no. 4, pp. 909-920, 2006.

[12] A. Vidal, F. D. Freijedo, A. G. Yepes, J. Malvar, O. Lopez, and J. Doval-Gandoy, Assessment and optimisation of the transient response of proportional-resonant current controllers for distributed power generation systems, IET Power Electron., vol. 6, no. 2, pp. 234-249, 2013.

[13] X. Yuan, W. Merk, H. Stemmler, and J. Allmeling, Stationary frame generalized integrators for current control of active power filters with zero steady-state error, IEEE Trans. Ind. Appl., vol. 38, no. 2, pp. 523-532, 2002.

[14] B. Beltran, T. Ahmed-Ali, and M. E. H. Benbouzid, High-order sliding-mode control of variable-speed wind turbines, IEEE Trans. Ind. Electron., vol. 56, no. 9, pp. 3314-3321, 2009.

International Journal of Engineering Research & Technology (IJERT)
ISSN: 2278-0181
Vol. 15 Issue 04 , April - 2026

[15] A. G. Aissaoui, A. Tahour, N. Essounbouli, F. Nollet, M. Abid, and M. I. Chergui, A fuzzy-PI control to extract an optimal power from wind turbine, Energy Convers. Manag., vol. 65, pp. 688-696, 2013.

[16] C. A. Rojas, J. Rodriguez, F. Villarroel, J. R. Espinoza, C. A. Silva, and M. Trincado, Predictive torque and flux control without weighting factors, IEEE Trans. Ind. Electron., vol. 60, no. 2, pp. 681-690, 2013.

[17] A. Rubaai, R. Kotaru, and M. D. Kankam, Online training of parallel neural network estimator-controller for induction motor drives, IEEE Trans. Ind. Appl., vol. 37, no. 5, pp. 1512-1521, 2001.

[18] K. S. Tey, S. Mekhilef, M. Seyedmahmoudian, B. Horan, A. T. Oo, and A. Stojcevski, Improved differential evolution-based MPPT algorithm using SEPIC for photovoltaic systems under partial shading conditions and load variation, IEEE Trans. Ind. Inform., vol. 14, no. 9, pp. 3862-3871, 2018.

[19] P. Kundur, Power System Stability and Control. New York: McGraw-Hill, 1994.

[20] I. Boldea, Variable Speed Generators. Boca Raton: CRC Press, 2006.

[21] F. Blaabjerg, Z. Chen, and S. B. Kjaer, Power electronics as efficient interface in dispersed power generation systems, IEEE Trans. Power Electron., vol. 19, no. 5, pp. 1184-1194, 2004.

[22] L. Zhang, L. Harnefors, and H.-P. Nee, Power-synchronization control of grid-connected voltage-source converters, IEEE Trans. Power Syst., vol. 25, no. 2, pp. 809-820, 2010.

[23] A. D. Hansen and G. Michalke, Fault ride-through capability of DFIG wind turbines, Renew. Energy, vol. 32, no. 9, pp. 1594-1610, 2007.